Structural and Reactivity Effects of Secondary Metal Doping into Iron-Nitrogen-Carbon Catalysts for Oxygen Electroreduction

Fang Luo, Aaron Roy, Moulay Tahar Sougrati, Anastassiya Khan, David Cullen, Xingli Wang, Mathias Primbs, Andrea Zitolo, Frédéric Jaouen, Peter Strasser

Structural and Reactivity Effects of Secondary Metal Doping into Iron-Nitrogen-Carbon Catalysts for Oxygen Electroreduction

Fang Luo[1], Aaron Roy[2], Moulay Tahar Sougrati[2], Anastassiya Khan[3], David A. Cullen[4], Xingli Wang[1], Mathias Primbs[1], Andrea Zitolo[3*], Frédéric Jaouen[2*] and Peter Strasser[1*]

[1]*Department of Chemistry, The Electrochemical Catalysis, Catalysis and Materials Science Laboratory, Chemical Engineering Division, Technical University Berlin, Straße des 17. Juni 124, 10623 Berlin, Germany*

[2] *ICGM, Univ. Montpellier, CNRS, ENSCM, 34293, Montpellier, France*

[3] *Synchrotron SOLEIL, L'Orme des Merisiers, Départementale 128, 91190 Saint-Aubin, France*

[4]*Center for Nanophase Materials Sciences, Oak Ridge National Laboratory, Oak Ridge, TN 37831, USA.*

* To whom correspondence should be addressed:

* e-mail: pstrasser@tu-berlin.de; frederic.jaouen@umontpellier.fr; andrea.zitolo@synchrotron-soleil.fr

Abstract

While improved activity was recently reported for bimetallic iron-metal-nitrogen-carbon (FeMNC) catalysts for the oxygen reduction reaction (ORR) in acid medium, the nature of active sites and interactions between the two metals are poorly understood. Here, FeSnNC and FeCoNC catalysts were structurally and catalytically compared to their parent FeNC and SnNC catalysts. While CO cryo-chemisorption revealed a twice lower site density of M-N_x sites for FeSnNC and FeCoNC relative to FeNC and SnNC, the mass activity of both bimetallic catalysts is 50-100% higher than that of FeNC, due to a larger turnover frequency in the bimetallic catalysts. Electron microscopy and X-ray absorption spectroscopy identified the coexistence of Fe-N_x and Sn-N_x or Co-N_x sites, while no evidence was found for binuclear Fe-M-N_x sites. ^{57}Fe Mössbauer spectroscopy revealed that the bimetallic catalysts feature a higher D1/D2 ratio of the spectral signatures assigned to two distinct Fe-N_x sites, relative to the FeNC parent catalyst. Thus, the addition of the secondary metal favored the formation of D1 sites, associated with the higher turnover frequency.

Introduction

Polymer Electrolyte Membrane fuel cell (PEMFC) has promising applications in future mobility and stationary power generation,[1-2] for which the catalysis of the electrochemical oxygen reduction reaction (ORR) plays a key role. Over the past decade, the broad class of metal-doped carbon-nitrogen materials (MNC) emerged as the most promising alternative to platinum for catalyzing the ORR,[3-7] and single metal atom sites of the type M-N_x identified as the most active site.[8-15] Among 3d transition metals, Fe, Co, and Mn-based monometallic MNC catalysts have long shown promising catalytic ORR activity in acid environments, while SnNC recently joint as another promising candidate.[7, 9-11, 16-17] Despite dramatic advances in understanding the ORR reaction mechanisms of MNC materials, their activity still needs to be increased in order to favorably compete with platinum.[18-20] While there is still some room for improvement in the site density (SD) of M-N_x sites in MNC catalysts, this strategy for increasing the activity will be limited by the competing formation of metal clusters (with low or no ORR activity in acid medium) during pyrolysis. Novel MNC materials comprising M-N_x sites with enhanced turnover frequency (TOF) is therefore a promising path.

While bimetallic Pt-M catalysts have been developed and the mechanisms leading to enhanced ORR activity identified,[21-22] bimetallic MNC catalysts have hitherto been under-explored and their activity descriptors remain unclear.[23-26] In particular, there is a lack of detailed understanding of the metals' coordination, nature of active sites and interactions between the two metals.[9, 27-30] Bogdanoff's group reported higher ORR activity for CoSnNC and CoFeNC compared to the parent CoNC, which was attributed to changes in the carbon specific surface area.[28] Bimetallic FeCoNC catalysts have been the most studied metal combination for ORR catalysis among MNC materials.[9, 30-34] Zelenay's group reported lower initial ORR activity but improved durability in PEMFC for FeCoNC vs. the parent FeNC catalyst.[9] Atanassov's group reported improved four-electron ORR selectivity for FeMNC (M=Co, Cu, Ni, Mn), catalysts relative to FeNC, but similar or lower ORR activity.[29] Dai's group claimed the presence of binuclear FeCo-N_x active sites in FeCoNC, on the basis of EXAFS analysis.[30] More recently, FeNiNC revealed lower ORR activity and four-electron selectivity compared to FeNC,[35] while it shows improved intrinsic catalytic activity, selectivity and promising stability in CO_2 electroreduction reaction.[36] The bimetallic FeMNC system possesses tremendous potential to further boost the intrinsic catalytic activity at the atomic level, however still has unexplored areas which calls for more systematic multi-techniques analysis to decipher their reactivity trends.[37-38] This study addresses this unmet need.

Results and Discussion

Electrocatalyst synthesis and structural characterization

Metal precursors $FeCl_3$ & $SnCl_2$ or $FeCl_3$ & $CoCl_2$ were introduced during the polymerization of aniline in 0.5 M HCl solution together with the carbon support (Ketjen EC 600JC), resulting in a homogenous polyaniline-carbon network (Supplementary Fig. 1a-c). These catalyst precursors were pyrolyzed in N_2 at 900 °C, and then acid-washed and re-pyrolyzed several times (Methods in S.I). FeSnNC and FeCoNC have a partially graphitized structure and similar carbon morphologies, as shown by TEM images (Supplementary Fig. 1d,e). This agrees with X-ray diffraction (XRD) patterns, showing two broad peaks at 26.2° and *ca* 44°, corresponding to the (002) and (101) reflections of graphite (Supplementary Fig. 2a,b).

The XRD patterns also revealed the presence of (Fe-doped) SnO_2 in FeSnNC and α-FeCo as well as a minor amount of γ-Fe and α-Fe in FeCoNC (Supplementary Note 1, Supplementary Fig. 2c-2d). A precise identification of the metal speciation was obtained from Mössbauer and X-ray absorption spectroscopy (XAS), discussed later. Combined with the fact that the parent FeNC material showed no diffraction peak related to Fe (Figure S1d in Reference[17]), these facts suggest that the addition of cobalt enhances the formation of iron-rich clusters during pyrolysis.

FeSnNC and FeCoNC show similar specific surface area (381-391 $m^2\ g^{-1}$) as well as mesoporous and microporous volumes, as quantified from nitrogen sorption measurements (Supplementary Fig. 3). These values are all significantly lower than the corresponding values measured for the parent FeNC material, with e.g. 665 $m^2\ g^{-1}$ specific surface area (Supplementary Table 1, and Supplementary Table 7 of Ref[17]). The lower specific surface area for these bimetallic catalysts may in particular result from the enhanced formation of bimetallic particles during the first pyrolysis, compared to FeNC. Despite lower BET, their average graphitization is similar as that for FeNC (Supplementary Fig. 2e, f). In the case of FeSnNC, the minor signal assigned to Sn-based particles in the final catalyst does not preclude the existence of a high amount of (Fe)Sn based particles after the first pyrolysis, and that would have been acid-washed later on. The latter hypothesis is supported by the final metal contents, measured with inductively coupled plasma (Supplementary Table 1, Supplementary Note 2). The chemical composition of the catalysts was analyzed with X-ray photoelectron spectroscopy (XPS) (Supplementary Fig. 4, Supplementary Tables 2 and 3).

There is no significant difference in the relative concentration of each N-species in FeSnNC and FeCoNC (Supplementary Note 3), nor in the total N content (5.4-6.5 at %).

To identify the metal speciation in these catalysts, we resorted to ^{57}Fe and ^{119}Sn Mössbauer spectroscopies, and to XAS at the Fe, Sn and Co K-edges. ^{57}Fe Mössbauer spectra were recorded both at 5 K and at room temperature, since this can help distinguishing if a spectral component shows a superparamagnetic transition (e.g. for nanometric metallic Fe clusters). For ^{119}Sn Mössbauer spectroscopy, the acquisition was performed only at room temperature, since Sn does not form superparamagnetic compounds and the signal type (sextet or doublet) is therefore independent of the temperature used to acquire the spectrum.

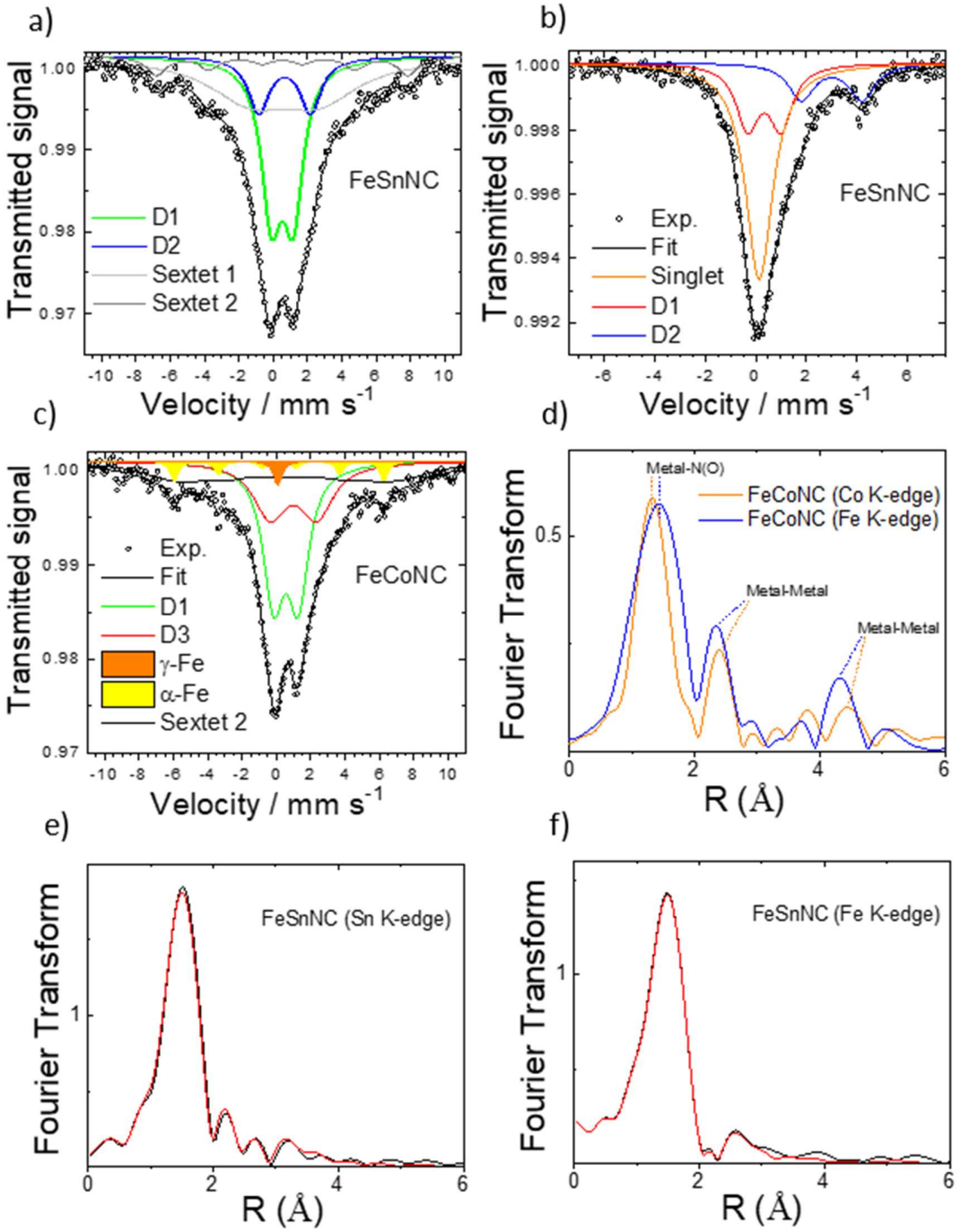

Figure 1. Characterization of Fe, Sn and Co coordination in FeSnNC and FeCoNC by Mössbauer and X-ray absorption spectroscopies. (a) ^{57}Fe Mössbauer spectrum at 5 K and (b) ^{119}Sn Mössbauer spectrum at 300 K for FeSnNC. (c) ^{57}Fe Mössbauer spectrum at 5 K for FeCoNC. The Mössbauer parameters for the fitted spectral components are shown in Supplementary Table 4. (d) Fourier transform of the experimental XAS spectra of FeCoNC at the Fe and Co K-edges. (e) Sn K-edge and (f) Fe K-edge EXAFS analyses in the Fourier transformed space of FeSnNC. Black and red curves in (e-f) are the experimental and theoretical spectra, respectively. The indicated radial distance is not corrected for phase-shift.

The ^{57}Fe Mössbauer spectrum of FeSnNC at 5 K was fitted with two doublets and two sextets (Figure 1a). These doublets, usually labelled D1 and D2 in the FeNC literature, are associated with different Fe-N_4 sites. Recent *in situ* and *post mortem* ^{57}Fe Mössbauer studies coupled with DFT concluded that D1 is likely a high-spin (HS) Fe(III)-N_4 site, with an oxygenated species adsorbed on Fe^{3+} [39-40,41] (Supplementary Note 4). D1 in FeSnNC accounts for 37 % of the signal, while D2 accounts for only 14% (Supplementary Table 4a, 5 K spectrum), much lower than the relative contribution of D2 in the parent FeNC (ca 60 %).[17] Combined ^{57}Fe Mössbauer-DFT studies assigned D2 to LS or MS Fe(II)-N_4 sites.[39-40] In addition, two sextets were identified, and the combined information from 5 K and 300 K spectra allows us assigning them to nanometric or amorphous oxidized iron particles (Supplementary Note 5, Supplementary Fig. 5), explaining also why they were not identified by XRD.

Overall, only ~50 % of the signal is assigned to Fe-N_4 sites in FeSnNC (37% D1 and 14% D2, at 5 K). In contrast, the parent FeNC material was shown to comprise all Fe atoms in the form of Fe-N_4 sites with a 40%/60% split for D1 and D2 sites (Figure S2 in Reference[17]). Thus, the Mössbauer results reveal the promotion of Fe clustering after the addition of tin, but also a much higher D1/D2 ratio in FeSnNC (37/14) relative to FeNC (40/60). The implications of this different distribution of Fe-N_x active sites are discussed later in the manuscript.

The ^{119}Sn Mössbauer spectrum of FeSnNC at 300 K was fitted with three components, two of which can be assigned to Sn(IV) sites (D1 and the singlet) and the third one (D2) to Sn(II) sites, on the basis of their distinct IS values (Figure 1b and Supplementary Table 4a). The parameters of these components are comparable to those recently reported by us for the parent SnNC material with Sn-N_x sites.[17] On the basis of calculated QS-values for different Sn-N_x moieties, we assigned D1 to O_2-Sn(IV)-N_x sites[17] and D2 to Sn(II)-N_x sites[17]. In all, the low Sn/Fe ratio in FeSnNC strongly suggests that the ORR activity of FeSnNC can mainly be ascribed to Fe-N_x sites.

The ^{57}Fe Mössbauer spectrum of FeCoNC at 5 K was fitted with five components (Figure 1c). The detailed discussion of these components can be found in Supplementary Note 6, and a summary is given here. D1 accounts for 40 % of the signal (Supplementary Table 4b), assigned to HS Fe(III)-N_4. The D2 component associated with LS or MS Fe(II)-N_4 is totally absent from FeCoNC, while it represented *ca* 60 % of the absorption area in the FeNC parent material (Figure S2 in Reference[17]). The D3 component is assigned to $FeCl_2 \cdot 4H_2O$.[42] A first sextet is assigned to α-Fe or α-FeCo alloy,[43]

while sextet 2 is assigned to $FeCoO_x$ superparamagnetic nanoparticles (Supplementary Fig. 5b). Overall, only ca 40 % of the signal is assigned to Fe-N_4 sites (D1) in FeCoNC. In contrast, the parent FeNC material was shown to comprise all Fe atoms in the form of Fe-N_4 sites with a 40%/60% split for D1 and D2 sites (Figure S2 in Reference[17]). Thus, akin to FeSnNC, the Mössbauer results reveal the promotion of Fe clustering after the addition of cobalt, and the further preferred formation of D1 sites relative to D2 sites, since we observe the complete absence of the D2 component in FeCoNC.

The local environments of Fe and Sn in FeSnNC were further investigated by modeling the *ex situ* EXAFS spectra at both the Fe and Sn K-edges. The result of the fitting is shown in Figure 1e-f, and Supplementary Figures 6-7, in the Fourier transformed (FT) and K-space, respectively. The first coordination shell around iron is well described by a Fe-N_4 moiety with a Fe-N bond length of 2.01 Å (Figure 1f and Supplementary Table 5). A second shell contribution is given by a Fe-C signal, with a fitted bond distance of 3.04 Å (Supplementary Table 5). This analysis is in good agreement with our previous structural characterization of PANI-derived FeNC catalysts,[44] but the higher Debye-Waller factor related to the carbon shell, indicates a disordered carbon structure around iron (Supplementary Table 5).

The experimental EXAFS spectrum of FeSnNC at the Sn K-edge was also fitted assuming a variable number of light elements (N or C, not distinguishable by EXAFS) in the plane containing the Sn atom, and a variable number of oxygen atoms in the axial position. The result of the fitting is shown in Figure 1e and Supplementary Fig. 7, revealing the dominant contribution of a first-shell peak associated with four in-plane N or C atoms at 2.03 Å, and of two axial oxygen atoms at 2.07 Å (Supplementary Table 6). The reminder of the FT-EXAFS spectrum is well reproduced by second-shell carbon atoms, and a minor Sn-Sn contribution with a fitted bond distance of 3.33 Å, suggesting that a minor amount of SnO_2 is present but it lacks long-range order or is (sub)nanometric (Supplementary Fig. 7, Supplementary Table 6). The X-ray absorption near edge structure (XANES) analysis is also in line with the presence of Sn(IV) species, with the threshold energy of the Sn K-edge XANES spectrum of FeSnNC being very close to that for Sn(IV)O_2 (Supplementary Fig. 8). This is in line with Sn(II) and Sn(IV) oxidation states and the major contribution of Sn(IV) species in the ^{119}Sn Mössbauer spectrum of FeSnNC (D1 and the singlet representing 83% of the signal, Supplementary Table 4a). Since there is no strong Sn-Sn contribution in the EXAFS signal corresponding to the second coordination shell (Figure 1f) it suggests that a minor amount of SnO_2 is present, which lacks long-range order or is nanometric.

Such nano-SnO_2 is compatible with the singlet component in the ^{119}Sn Mössbauer spectrum. The Sn-N in-plane bond distance of 2.03 Å is comparable to that determined by us in the parent SnNC material, 2.06 Å (Table S4 in Reference[17]), while the Sn-O axial distance is shorter in FeSnNC vs. SnNC (2.07 and 2.13 Å, respectively). This is however probably a bias due to the coexistence of a larger amount of nano-SnO_2 (with Sn-O bond as low as 2.05 Å[45]) in FeSnNC relative to SnNC. The larger amount of nano-SnO_2 is suggested from Mössbauer data and also supported by a higher Sn-O average coordination number in FeSnNC than in SnNC (2.0 and 1.0, respectively, Supplementary Table 6, and Table S4 in Reference[17]). Finally, it is important to note that the EXAFS analysis reveals the absence of Fe-Sn bonds in FeSnNC, thereby supporting that Fe-N_x and Sn-N_x moieties are separate and do not form binuclear Fe-Sn-N_x sites.

Regarding the *ex situ* EXAFS analysis of FeCoNC, the Fe and Co K-edge FT-EXAFS spectra shown in Figure 1d reveal first-shell peaks at 1.3 and 1.4 Å (not corrected for phase shift), assigned to Fe-N_x and Co-N_x moieties, respectively.[10-11] Both the Fe and the Co K-edge spectra also reveal the presence of metal-based nanoparticles, evidenced by significant metal-metal interactions (Fe-Fe, Co-Co or Fe-Co), with bond distances compatible with a metallic structure. This agrees with XRD and ^{57}Fe Mössbauer results. Therefore, we do not see experimental evidence for the presence of binuclear Fe-M-N_x sites (M = Sn or Co) in the present bimetallic materials. This does not preclude the existence of such sites for bimetallic materials prepared differently. Binuclear Fe-Co-N_x active sites embedded in nitrogen-doped carbon was demonstrated earlier to gain high ORR activity,[25] while how the two metal atoms transform to active sites primarily rely on the sources of M, N and C, as well as synthesis strategies and pyrolysis process.

The carbon morphology and metal dispersion in FeSnNC and FeCoNC was further investigated with scanning transmission electron microscopy (STEM). Aberration-corrected annular dark-field (ADF) STEM images reveal the homogeneous dispersion of single metal atom sites based on Fe, Sn and Co within graphene planes (Figure 2). FeSnNC and FeCoNC consist of a primary carbon matrix and secondary few-layer graphene sheets (Supplementary Fig. 9-10). Graphene-like structures were previously reported for PANI-derived MNC catalysts comprising Fe.[9, 46-47] The presence of single metal atoms (dots exhibiting bright contrast) was confirmed in the ADF-STEM images, with no apparent metal clusters or nanoparticles. Having a significantly larger atomic number, the brighter Sn atoms could be distinguished from Fe in the ADF-STEM images (Supplementary Fig. 9), which was confirmed by electron energy loss spectroscopy (EELS) (Figure 2a-d). Fe and Co cannot be distinguished from each other with ADF-STEM, but EELS detected

both elements at the single atom level (Figure 2e-h). Due to the weak EELS signal combined with the instability of the single atoms under the electron beam, it was impossible to determine the valence state of the individual metal atoms. EEL spectra obtained from the single atoms also routinely contained a nitrogen peak, suggesting coordination of N with Fe, Sn and Co (Figure 2). Besides single metal atoms, electron microscopy could also detect few metal-based nanoparticles randomly distributed within FeSnNC and FeCoNC catalysts (Supplementary Fig. 11), in line with XRD, EXAFS and Mössbauer analyses.

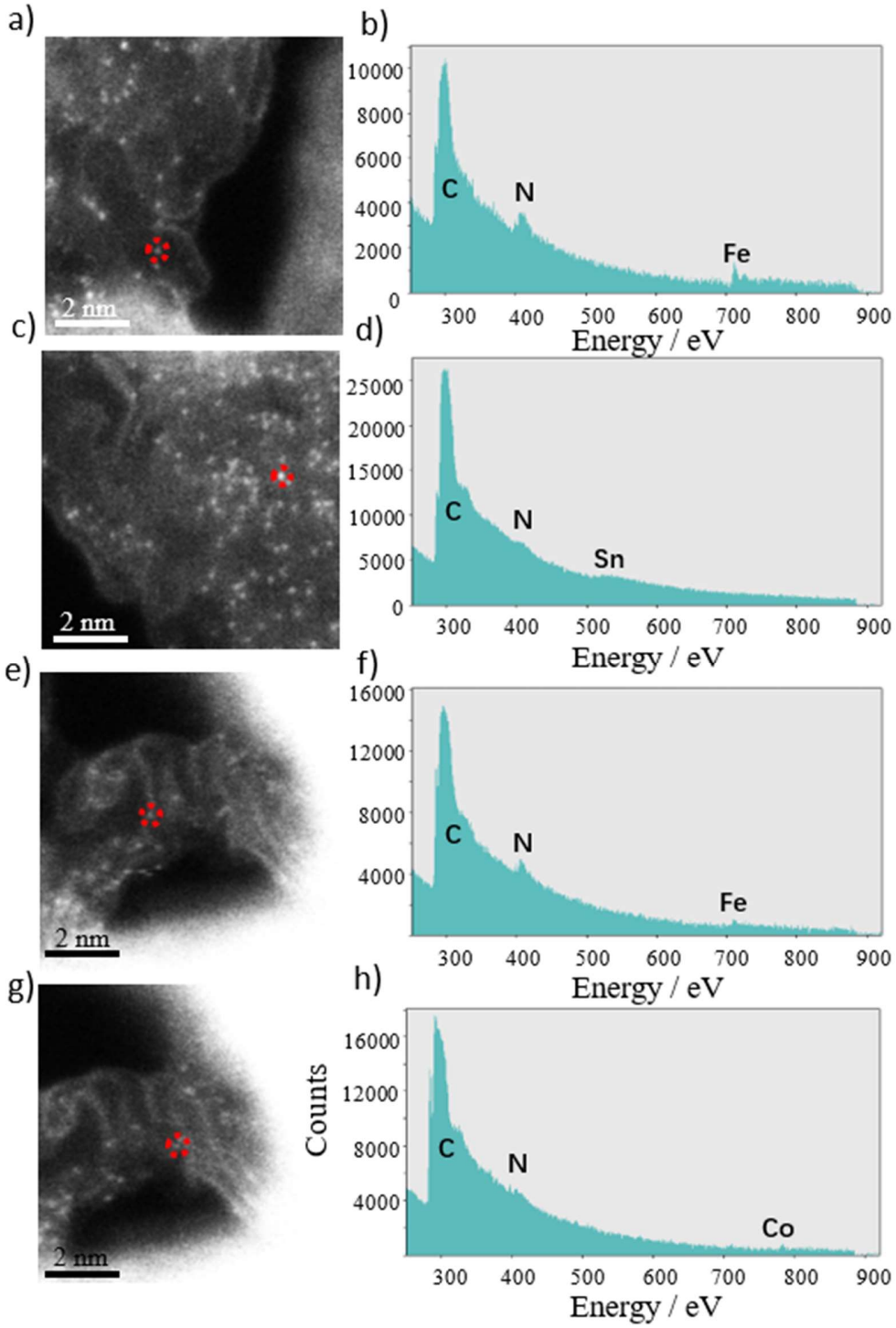

Figure 2. Characterization of atomically dispersed Fe, Sn and Co atoms in FeSnNC and FeCoNC by STEM-EELS. (a, c, e, g) Atomic resolution ADF-STEM images of metal atoms homogeneously distributed across the carbon surface with (b, d, f, h) EEL spectra of C, N K-edges, Fe, Co L-edges and Sn M-edge acquired from single atoms (red circles) in few-layer graphene demonstrating the presence of N around the Fe, Sn and Co atoms for (a-d) FeSnNC and (e-h) FeCoNC.

Electrochemical Oxygen-reduction activity and selectivity

The electrocatalytic activity and selectivity for ORR were measured using a Rotating Ring Disk Electrode (RRDE) in 0.1 M $HClO_4$ electrolyte (Figure 3). Representative polarization curves shown in Figure 3a reveal that both bimetallic catalysts show enhanced activity compared to their parent FeNC material.[17, 48] The catalytic ORR activity was quantified using a Koutecky-Levich analysis. Representative Tafel plots are shown in Supplementary Fig. 12. The beginning-of-life mass activity at 0.8 V vs. RHE averaged over multiple experiments is shown in Figure 3b, suggesting a two-fold higher initial activity of FeSnNC vs. FeNC, and a 50% enhancement of FeCoNC vs. FeNC. The enhancement in ORR activity of FeSnNC and FeCoNC is even higher when compared to SnNC and CoNC (Figure 3b). These trends can be rationalized by the similar TOF of Sn-N_x and Fe-N_x sites, yet lower SD of SnNC compared to FeNC, and by the lower TOF of Co-N_x moieties vs. Fe-N_x moieties.[17, 49-50] Note that the bimetallic FeSnNC and FeCoNC catalysts showed a clearly higher mass activity than four benchmark PGM-Free FeNC catalysts[48] (see Figure 6a from reference[48]) and was equally active to other recent reports on advanced MNC materials.[30, 50-51] The high selectivity was confirmed with RRDE (Figure 3a), FeSnNC being slightly more selective than FeCoNC and FeNC.

In summary, FeSnNC and FeCoNC are significantly more active than the parent FeNC material. For FeSnNC, the strong increase in mass activity relative to FeNC is surprising in view of the low amount of Sn. The increased mass activity of FeCoNC is surprising, as well, given the presence of Fe and/or Co clusters versus the absence of such clusters in the FeNC parent material. To better understand the reasons for the increased mass activity, we moved to quantify the SD and TOF of the bimetallic catalysts.

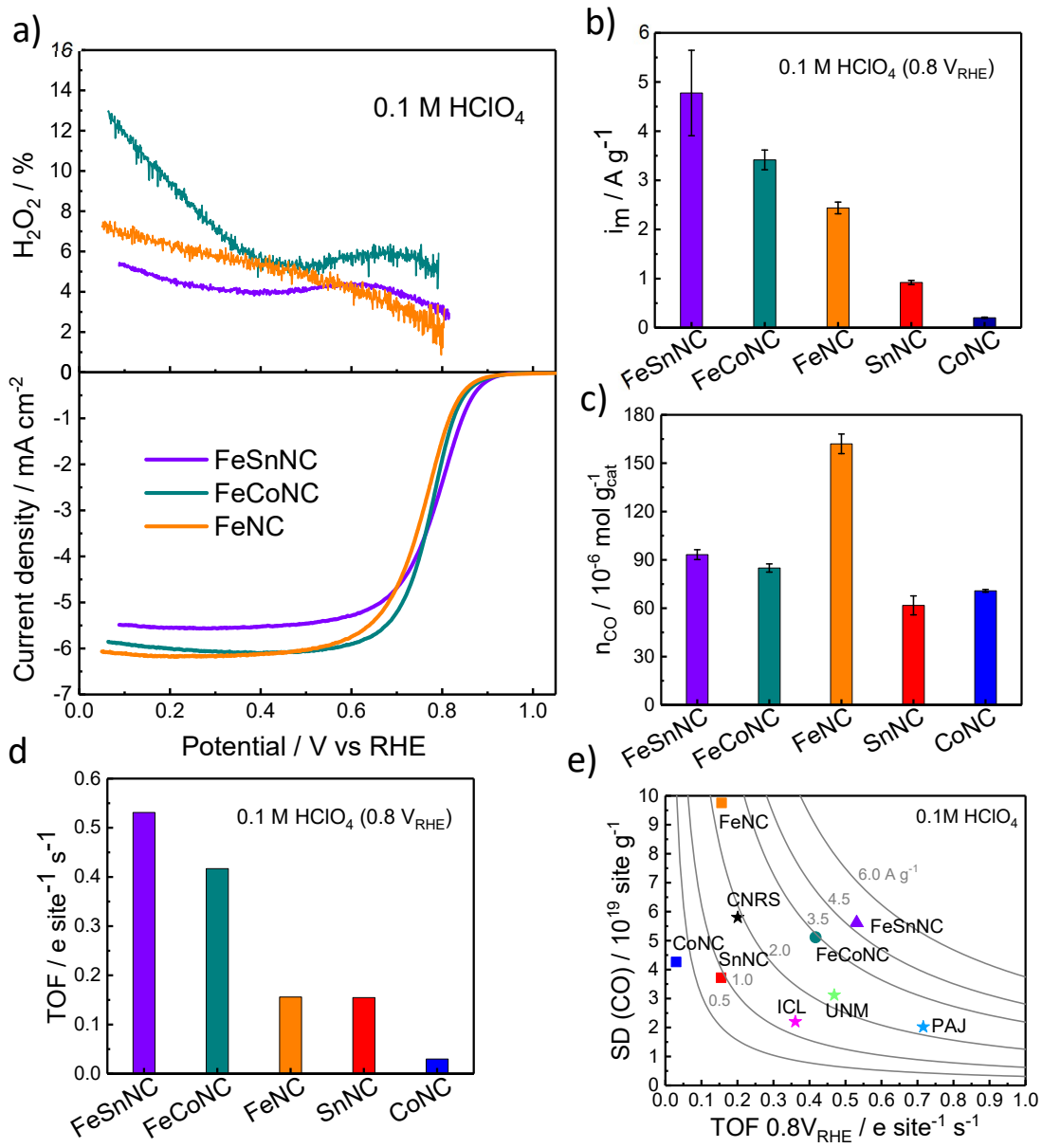

Figure 3. Electrochemical ORR activity, selectivity, active site density, TOF, and SD-TOF reactivity map. (a) ORR linear Scan Voltammetry (LSV), H_2O_2 yield of the two bimetallic catalysts and of the parent FeNC material in oxygen-saturated acidic electrolyte. (b) Comparison of average ORR mass activity at 0.8 V_{RHE} for the two FeSnNC and FeCoNC bimetallic catalysts, the parent FeNC and SnNC monometallic catalysts and a CoNC single-atom-site material derived from ZIF-8. The average activity is derived from multiple RRDE experiments performed at 1600 rpm, in O_2-saturated 0.1 M $HClO_4$, 25 °C, with a geometric catalyst loading of 0.8 $mg_{MNC} \cdot cm^{-2}$. The ORR mass activity of SnNC, FeNC and CoNC at 0.8 V_{RHE} are taken from Figure S6 in Reference[17]. (c) Gravimetric molar CO uptake of catalysts. The data for FeNC, SnNC and CoNC was reproduced from Figure 2c in Reference[17]. (d) Comparison of TOF values for ORR at 0.8 V_{RHE}. The TOF of FeNC, SnNC and CoNC was reproduced from Figure 2e in Reference[17]. (e) Hyperbolic iso-mass-activity curves in SD-TOF activity maps, as calculated by applying Supplementary Equation 9, and

the experimental data points measured for FeSnNC and FeCoNC at 0.8 V vs. RHE, for FeNC, SnNC and CoNC (data taken from Reference[17]) and for other FeNC catalysts labelled as CNRS, UNM, ICL and PAJ (data taken from Figure 6a in Reference[48]).

Deconvolution of the mass activity into SD and TOF and reactivity maps

The surface site density, SD, was measured using the previously developed and validated CO cryo-chemisorption technique. CO adsorbs to single metal active sites of pyrolyzed Fe, Co, and SnNC catalysts at 193 K.[17, 48, 52-53] The quantification of the amount of adsorbed CO per mass of MNC allows estimation of SD, assuming one CO molecule binds per M-N_x active site. The CO cryo-chemisorption method was successfully applied to quantify Fe-N_x, Co-N_x, Mn-N_x, Sn-N_x, Cu-N_x sites in monometallic MNC materials.[17, 54]. The co-presence of metal-based particles in FeCoNC and FeSnNC could potentially bias the counting of the single metal active sites, if some CO adsorbs on such particles. To assess this possibility, we measured the CO uptake and CO TPD on a range of iron species (iron was chosen since it binds CO strongest among Fe, Co and Sn) and no CO adsorption could be detected on pure metallic iron, iron oxides, or sulfides (Supplementary Fig.13). Thus, we can conclude that the CO technique is specific for M-N_x sites in FeCoNC and FeSnNC, but the measured SD corresponds to the sum of Fe-N_x and either Sn-N_x sites or Co-N_x sites. In turn, this implies that the TOF (obtained from the ratio between the overall mass activity and the SD (Supplementary Equations 5 and 9) corresponds to a mean TOF averaged over all M-N_x sites. Both FeSnNC and FeCoNC adsorb significant amount of CO, as evidenced by the lower signal for the first pulses (Supplementary Fig. 14). The total CO uptake, and hence the SD, is quantified from the 6 CO pulses (see Supplementary Information – CO Pulse Chemisorption section). The analysis shows that FeSnNC adsorbs more CO than FeCoNC ($93 \cdot 10^{-6}$ and $85 \cdot 10^{-6}$ mol·g^{-1}, respectively) (Figure 3c). Compared to the parent monometallic catalysts, both FeSnNC and FeCoNC adsorb significantly less CO than FeNC ($162 \cdot 10^{-6}$ mol·g^{-1}), but more than CoNC ($71 \cdot 10^{-6}$ mol·g^{-1}) and SnNC ($62 \cdot 10^{-6}$ mol·g^{-1}) (Figure 3c, Supplementary Table 7a). This is in qualitative agreement with the EXAFS and Mössbauer spectroscopy characterization, showing that the addition of Sn, and especially Co, promoted single metal atom aggregation during pyrolysis.

Next, average TOF values at 0.8 V_{RHE} were derived from experimental ORR catalyst mass activity and experimental SD values (Supplementary Fig. 15). FeSnNC showed a slightly higher TOF than FeCoNC, while both bimetallic materials had a significantly higher TOF than their parent FeNC, SnNC, or CoNC catalysts (Figure 3d, Supplementary Table 7a). The TOF of FeSnNC was more

than 3-fold higher than that of FeNC. This is particularly intriguing and interesting, since the FeSnNC mainly comprises Fe-N_x active sites, and only a minute amount of Sn-N_x sites. The total number of Fe and Sn atoms in FeSnNC is $3.42 \cdot 10^{20}$ atoms$\cdot g^{-1}$ (Supplementary Table 7a) and in this, only about 2%, i.e. $0.07 \cdot 10^{20}$ atoms$\cdot g^{-1}$, are Sn. We note that Sn-N_x sites in monometallic SnNC showed comparable TOF to Fe-N_x sites in monometallic FeNC.[17] Therefore, our present analysis suggests an enhancement in the TOF of the Fe-N_x sites in the bimetallic FeSnNC catalyst relative to those in FeNC, which can hardly be explained by a direct synergistic effect between the Fe-N_x and the 2% Sn-N_x sites. Moreover, EXAFS did not support the presence of binuclear Fe-Sn-N_x sites. The analysis is more difficult for FeCoNC, due to balanced amounts of Fe and Co and due to the fact that the material also comprises a significant amount of metallic Fe, Co or FeCo particles. Nevertheless, there is no experimental support for the presence of binuclear Fe-Co-N_x sites in FeCoNC either, and the TOF of Co-N_x sites in CoNC is much lower than that of Fe-N_x sites in FeNC.[17] Therefore, the present analysis likewise suggests that the TOF of Fe-N_x sites in FeCoNC was increased via the addition of cobalt in the synthesis. We also assessed the overall utilization factor, defined as the ratio of SD to the sum of all metal atoms present in the materials (Supplementary Table 7a). The overall utilization factors for FeSnNC and FeCoNC are similar (0.14-0.16), and only slightly lower than those of the parent FeNC and SnNC catalysts (0.19-0.23). The slight decrease in overall utilization for the bimetallic catalysts is accounted for by the presence of metal clusters, unlike in FeNC and SnNC. The higher overall utilization factor for CoNC compared to all others is ascribed to the distinct synthesis from ZIF-8, while all other materials in Supplementary Table 7a were prepared via a polyaniline approach.

Overall, the favorably high mass activity of FeSnNC and FeCoNC over monometallic reference catalysts is caused by enhancements of the TOF (2.7-3.4x), despite lower SD (0.52-0.57x). The possibility to raise the TOF of Fe-N_x sites by the addition of a second metal is of fundamental and practical importance, but the results also show the importance of re-optimizing the synthesis to mitigate the formation of iron clusters. The SD-TOF reactivity map (Figure 3e) provides a snapshot of the progress achieved with the bimetallic FeSnNC and FeCoNC catalysts compared to (i) the parent FeNC and SnNC materials, (ii) other benchmark FeNC catalysts prepared (Supplementary Table 7b). The map demonstrates the enhanced activity of FeCoNC and FeSnNC as a result of an increased TOF at acceptable SD. In particular, the FeSnNC material reaches an activity close to the target of 6.6 A$\cdot g^{-1}$, as defined by the ElectroCat network funded by the US Department of Energy and the EU projects CRESCENDO and PEGASUS funded by the Fuel Cells and Hydrogen Joint Undertaking.[55-57]

Single-cell PEMFC results

The activity and performance of FeSnNC and FeCoNC were finally evaluated in single-cell PEMFC, and compared to that of the reference FeNC material. In addition, we also evaluated the PEMFC performance of these three catalysts after a short treatment at 750°C under flowing NH_3 (labelled as MNC-NH_3). Such an NH_3 treatment did not alter the metal speciation of monometallic MNCs, while boosting their ORR activity and performance in PEMFC.[17] Some work reported that NH_3 treatments increased the micropore surface area as well as the Lewis basicity of the MNC surface.[11, 40] Using *ex situ* XAS measurements, we verified that the Fe, Sn and Co speciation of FeSnNC and FeSnNC-NH_3 as well as of FeCoNC and FeCoNC-NH_3 remained essentially identical (Supplementary Fig. 16). This suggests carbon matrix Lewis basicity as the main origin of the ORR improvements of NH_3-treated samples, while the nature and number of active sites was not affected. Figure 4a shows a moderately improved ORR activity of FeSnNC *vs.* FeCoNC at 0.8 V and above, in line with RDE results. The higher cell performance of FeSnNC *vs.* FeCoNC was most evident at larger current densities, where the cell performance was controlled by both ORR kinetics and ohmic or mass-transport losses. The single-cell performance based on FeSnNC-NH_3 and FeCoNC-NH_3 cathodes showed significantly enhanced kinetic performance below 600 mA cm^{-2} compared to the untreated catalysts. The higher performance is mainly due to improved ORR kinetics, as an analysis of the TOF in PEMFC suggests. The TOF_{PEMFC} value of FeSnNC-NH_3 was 2.5 e $site^{-1}$ s^{-1}, compared to 0.6 e $site^{-1}$ s^{-1} for FeSnNC catalyst, as derived from mass-normalized cell current densities at 0.8 V iR-corrected cell voltage in PEMFC experiments and from the average SD derived using CO cryo-chemisorption (Supplementary Equation 10). Figure 4b shows the iR-corrected Tafel plots, demonstrating a kinetic improvement of at least five-fold at 0.8 V cell potential, thanks to the NH_3 treatment. The comparison to the reference FeNC material is shown in Supplementary Fig. 17. FeSnNC and FeCoNC showed higher ORR activity and cell performance than FeNC and FeNC-NH_3. In conclusion, our PEMFC data demonstrate the impressive kinetic benefits of the bimetallic catalysts in a cell environment. The liquid electrolyte RDE data obviously transfer into the PEMFC environment.

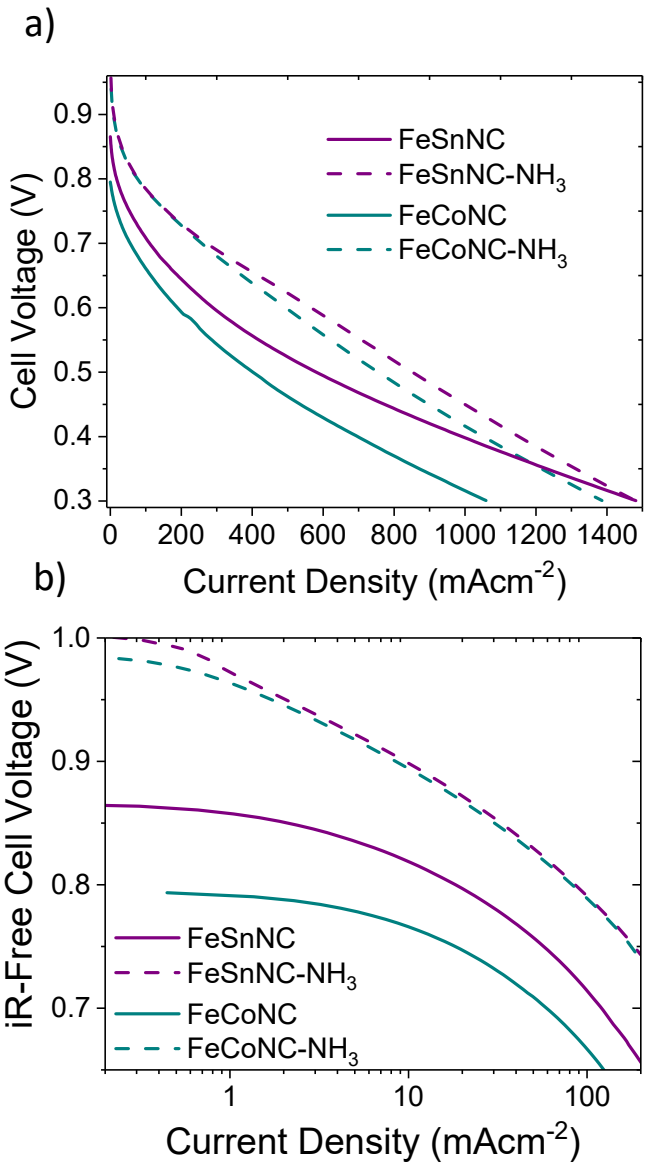

Figure 4. Single-cell PEMFC results for bimetallic catalysts and NH_3-treated bimetallic catalysts. a) as-measured polarization curves and b) iR-corrected Tafel plots. The cathode loadings were 4 $mg \cdot cm^{-2}$ with anode loadings of 2.0 $mg_{Pt} \cdot cm^{-2}$. The cell was at 80°C, pure H_2 and O_2 at 100% relative humidity at 2 bar absolute pressure. Polarization curves were acquired using linear scan voltammetry with a scan rate of 1 $mV \cdot s^{-1}$. The NH_3 pyrolysis was performed at 750°C.

Operando XANES signature of Fe-N_x, Sn-N_x, and Co-N_x moieties in bimetallic MNCs

Operando XAS experiments were conducted in N_2-saturated electrolyte on FeSnNC, FeSnNC-NH_3, FeCoNC and FeCoNC-NH_3 at the Fe, Sn and Co K-edges. This is the first *operando* report on Sn K-edge XANES spectra of single-metal-atom Sn-N_x sites. As the electrode potential was lowered, spectral changes at the Fe K-edge became evident for FeSnNC (Figure 5a), which resembled Fe-N_x sites trends in aqueous acidic electrolyte.[11] The change in XANES threshold energy with potential indicated a Fe(III)/Fe(II) redox transition, while changes in spectral features revealed a structural modification of a significant fraction of Fe-N_x sites in the region 0.2-0.9 V_{RHE}. A similar trend of XANES spectral changes with electrochemical potential was observed for the parent FeNC material (Supplementary Fig. 18a). A detailed comparison shows that the Fe K-edge XANES spectra of FeSnNC and the parent FeNC are identical at 0.9 V_{RHE} (Supplementary Fig. 18b), while a small shift to higher energy was observed for FeSnNC *vs.* FeNC at 0.4 and 0.2 V_{RHE} (Supplementary Fig. 18c-d). This suggests a higher mean Fe oxidation state in FeSnNC than in FeNC in the low potential regime, while no difference was observed at 0.9 V and also at any potential above 0.6 V vs. RHE (not shown). In contrast, the Sn K-edge XANES spectra of FeSnNC showed no dependence on the electrode potential over the entire potential range (Figure 5b), and the same was found true for SnNC (Supplementary Fig. 19). The potential-independence evidences that Sn cations in Sn-N_x sites do undergo no change in structure and oxidation state in the ORR potential range, akin to Co-N_x sites in CoNC.[10]

After NH_3-treatment, similar *operando* XANES trends were observed. With varying electrode potentials, the FeSnNC-NH_3 catalyst showed electronic and structural changes at the Fe K-edge that were similar to those of untreated FeSnNC (compare Figure 5a and Supplementary Fig. 20). A deeper inspection of the *operando* Fe K-edge XANES spectra showed a remarkable positive shift in the edge position of FeSnNC-NH_3 with respect to FeSnNC (0.25 eV at 0.9 V *vs*. RHE), which is even more distinctive at low potentials (0.4 eV at 0.2 V *vs*. RHE) (Supplementary Fig. 21). This indicates a higher mean Fe oxidation state in FeSnNC-NH_3 under applied potentials, quite similar to the findings of FeSnNC above.

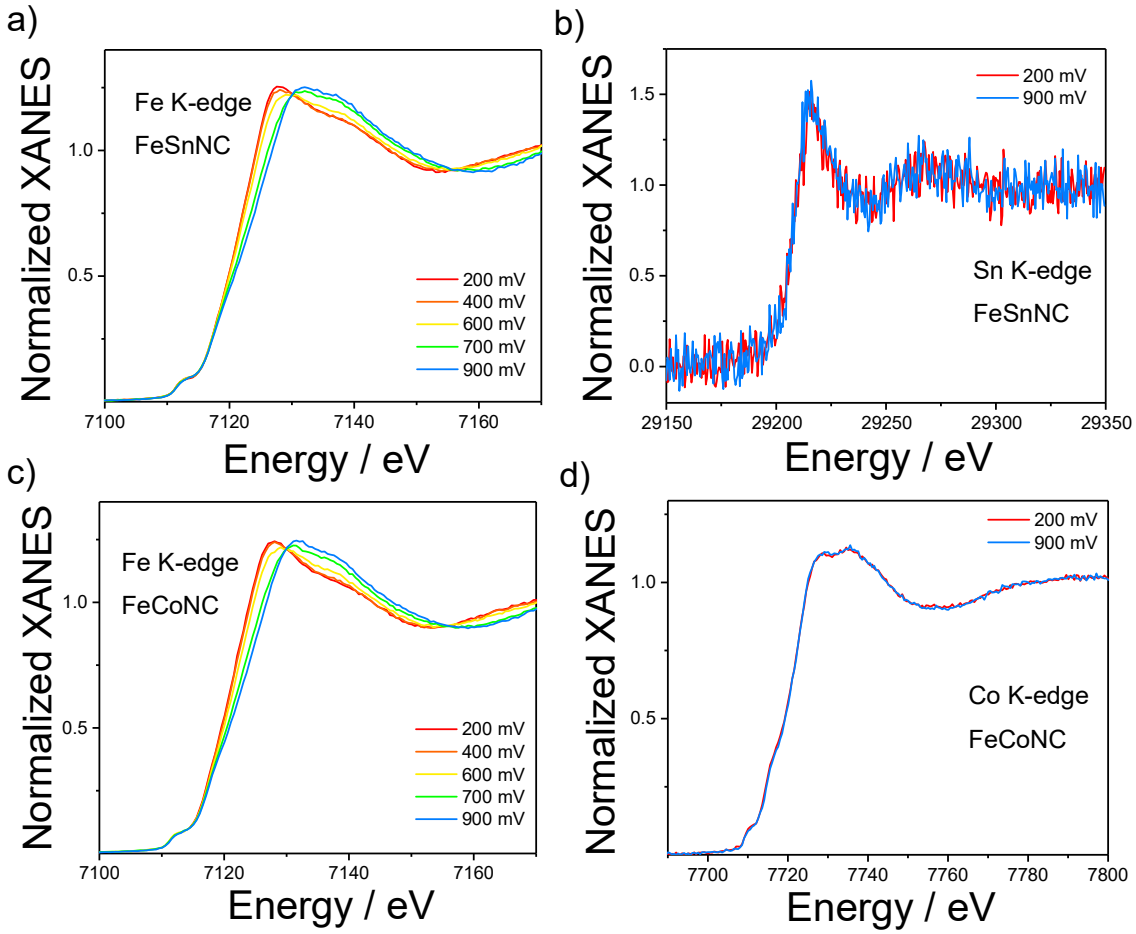

Figure 5. (a) Fe K-edge XANES spectra of FeSnNC as a function of the electrochemical potential; (b) Sn K-edge XANES spectra of FeSnNC at 900 mV (blue curve) and 200 mV (red curve); (c) Fe K-edge XANES spectra of FeCoNC as a function of the electrochemical potential; (d) Co K-edge XANES spectra of FeCoNC at 900 mV (blue curve) and 200 mV (red curve).

Since the trend of ORR activity observed in PEMFC is FeSnNC-NH_3 >> FeSnNC > FeNC (Figure 4), the *operando* XANES data therefore suggests a positive correlation between ORR activity (TOF of Fe-N_x sites) at 0.8 V vs. RHE and the edge position of *operando* Fe K-edge XANES spectra measured at a given potential. This is confirmed by plotting the current density measured at 0.8 V iR-free PEMFC voltage vs. the energy shift ΔE of the *operando* threshold XANES spectra measured at 0.4 V vs. RHE (Supplementary Fig. 22). The current density of FeSnNC-NH_3 and FeSnNC at 0.8 $V_{iR\text{-}corrected}$ were 90 and 20 mA cm^{-2}, respectively, exceeding the 2.7 mA cm^{-2} value for FeNC measured under the same conditions.[17] Similar correlations were observed if the *operando* XANES energy shift ΔE at the Fe K-edge was considered at varying electrode potentials (see the Table inside Supplementary Fig. 22a). The trend also holds when the TOF is considered,

rather than the overall ORR activity (Supplementary Fig. 22b). From these findings we conclude that the enhanced intrinsic catalytic reactivity (TOF) is associated, possibly even originates, from the higher mean oxidation state of the active Fe-N_x sites in the bimetallic catalysts.

The XANES spectra of FeCoNC and FeCoNC-NH_3 at the Fe K-edge showed potential-dependent spectral changes that were quantitatively very similar to those observed for the parent FeNC and the FeSnNC materials (Figure 5c and Supplementary Fig. 23a). By contrast, no spectral Co K-edge changes with potential were observed for FeCoNC and FeCoNC-NH_3 (Figure 5d and Supplementary Fig. 23b). This is consistent to the parent CoNC catalyst, the Co-N_x spectra of which behaved independent of potential.[10] On the down side, the significant presence of low valent Fe particles in FeCoNC and FeCoNC-NH_3 revealed by EXAFS prevents the accurate detection of electronic effects on Fe-N_x sites (if any) induced by the presence of cobalt centers (Supplementary Fig. 24-25, Supplementary Note 7).

Finally, we discuss how the addition of the secondary metal Sn or Co may lead to a higher ratio of D1/D2 species (*ex situ* ^{57}Fe Mössbauer) or higher average oxidation state of Fe at a given potential (*operando* XANES), both phenomena associated with the higher TOF. The negative trend between the D2/D1 ratio and the TOF is shown in Supplementary Fig. 26 (the D1/D2 ratio could not be used for the plot, as this would result in infinite values for FeCoNC which contains no D2 signal). The selective formation of D1 vs. D2 sites may originate from (i) a modified carbon structure triggered by the presence of the secondary metal dopant, (ii) competition between iron and the secondary metal dopant for the 'D2 sites', or (iii) different pyrolysis trajectories induced by the presence of the secondary metal. The hypothesis (i) is related to increased disorder in the carbon matrix in presence of the second metal dopants. The D1 Fe motif is typically associated with an FeN_4C_{12} porphyrinic site, and its formation requires more disorder in the carbon matrix than the D2 motif, which is associated with a FeN_4C_{10} structure. The hypothesis (ii) is related to the possibility that the apparent effective selective formation of D1 sites in these bimetallic materials is actually an indirect effect resulting from different affinities of the MN_4C_{10} and MN_4C_{12} structures for Fe versus Sn or Co cations. The hypothesis (iii) is related to the transient species formed during pyrolysis. Catalytic precursors containing $FeCl_2$ evolve to Fe-N_x active sites via the formation of α-Fe_2O_3 at relatively low temperature, which subsequently transforms into tetrahedral Fe(II)-O_4 oxide between room temperature and 600 °C.[58] The presence of an additional metal could trigger the formation of Sn- and Co-doped Fe_2O_3 with distinct structural and magnetic properties,[59-60] thus

modifying the Fe-N_x synthesis pathway, possibly leading to the preferential formation of Fe-N_x moieties associated with the D1 signal (Supplementary Note 8).

Conclusions

The present work establishes that the TOF of Fe-N_x sites is significantly increased by the addition of a secondary metal atom, such as Sn or Co, and that binuclear sites with adjacent M-M or M-N-M motifs were absent in these bimetallic catalysts. ^{57}Fe Mössbauer spectroscopy identified a significantly larger ratio of Fe(III)-N_x/Fe(II)-N_x sites (D1/D2 ratio) in both bimetallic catalysts, relative to FeNC. The increased intrinsic TOF of bimetallic catalysts originates from this enhanced relative abundance of Fe D1 site.

Supporting Information

Additional figures for TEM, XRD, N_2 sorption, XPS, Mössbauer spectra, XAS, CO adsorption and TPD data, supporting electrochemical characterization and additionnal Tables of pore size distribution, elemental content analysis, Mössbauer spectra fittings, EXAFS fittings, TOF and SD data.

Author Information

Corresponding authors: pstrasser@tu-berlin.de; frederic.jaouen@umontpellier.fr; andrea.zitolo@synchrotron-soleil.fr

Acknowledgements

The authors would like to acknowledge Dr. Sören Dresp, Dr. Shuang Li, Dr. Huan Wang and Dr. Tobias Reier for assistance with RRDE, XPS, nitrogen physisorption and CO pulse chemisorption experiments. We also thank Prof. Ulrike I. Kramm for help with Mössbauer spectroscopy measurements. Aberration-corrected STEM-EELS was conducted at the Center for Nanophase Materials Sciences, which is a US Department of Energy Office of Science User Facility, at Oak Ridge National Laboratory. This project received partial financial support by the Graduate School of Excellence Energy Science and Engineering (GRC1070). The research leading to some of these results has received funding from the Fuel Cells and Hydrogen 2 Joint Undertaking under grant agreement No 779366. This Joint Undertaking receives support from the European Union's Horizon 2020 research and innovation program, Hydrogen Europe and Hydrogen Europe research. A. Z and A. K acknowledge support from the French ANR project ANR-19-CE05-0006 (SPECTROSCOPE), and Synchrotron SOLEIL (Gif-sur Yvette, France) for provision of synchrotron radiation facilities at beamline SAMBA (proposal number 20201432). F. L., M. P. and

P. S. acknowledge financial support by the Bundesministerium für Bildung und Forschung (BMBF) under The German Israeli Battery and Fuel Cell program, FKZ 03XP0251.

References

1. Steele, B. C. H.; Heinzel, A., Materials for fuel-cell technologies. *Nature* 2001, *414*, 345.
2. Badwal, S. P.; Giddey, S. S.; Munnings, C.; Bhatt, A. I.; Hollenkamp, A. F., Emerging electrochemical energy conversion and storage technologies. *Frontiers in chemistry* 2014, *2*, 79.
3. Jaouen, F.; Proietti, E.; Lefèvre, M.; Chenitz, R.; Dodelet, J.-P.; Wu, G.; Chung, H. T.; Johnston, C. M.; Zelenay, P., Recent advances in non-precious metal catalysis for oxygen-reduction reaction in polymer electrolyte fuelcells. *Energy Environ. Sci.* 2011, *4* (1), 114-130.
4. Bashyam, R.; Zelenay, P., A class of non-precious metal composite catalysts for fuel cells. *Nature* 2006, *443* (7107), 63-66.
5. Chung, H. T., and Zelenay, P Non-precious metal catalysts prepared from precursors comprising cyanamide and polyaniline. US Patent 9,979,026 B2, May 22, 2018.
6. Sahraie, N. R.; Kramm, U. I.; Steinberg, J.; Zhang, Y.; Thomas, A.; Reier, T.; Paraknowitsch, J. P.; Strasser, P., Quantifying the density and utilization of active sites in non-precious metal oxygen electroreduction catalysts. *Nature communications* 2015, *6*, 8618.
7. Lefèvre, M.; Proietti, E.; Jaouen, F.; Dodelet, J.-P., iron-Based Catalysts with Improved Oxygen Reduction Activity in Polymer Electrolyte Fuel Cells. *Science* 2009, *324*, 71-74.
8. Martinez, U.; Komini Babu, S.; Holby, E. F.; Chung, H. T.; Yin, X.; Zelenay, P., Progress in the Development of Fe-Based PGM-Free Electrocatalysts for the Oxygen Reduction Reaction. *Advanced materials* 2019, e1806545.
9. Wu, G.; More, K. L.; Johnston, C. M.; Zelenay, P., High-Performance Electrocatalysts for Oxygen Reduction Derived from Polyaniline, Iron, and Cobalt. *Science* 2011, *332* (6028), 443-447.
10. Zitolo, A.; Ranjbar-Sahraie, N.; Mineva, T.; Li, J.; Jia, Q.; Stamatin, S.; Harrington, G. F.; Lyth, S. M.; Krtil, P.; Mukerjee, S.; Fonda, E.; Jaouen, F., Identification of catalytic sites in cobalt-nitrogen-carbon materials for the oxygen reduction reaction. *Nature Communications* 2017, *8* (1), 957.
11. Zitolo, A.; Goellner, V.; Armel, V.; Sougrati, M.-T.; Mineva, T.; Stievano, L.; Fonda, E.; Jaouen, F., Identification of catalytic sites for oxygen reduction in iron- and nitrogen-doped graphene materials. *Nat Mater* 2015, *14* (9), 937-942.
12. Chen, Y.; Ji, S.; Zhao, S.; Chen, W.; Dong, J.; Cheong, W. C.; Shen, R.; Wen, X.; Zheng, L.; Rykov, A. I.; Cai, S.; Tang, H.; Zhuang, Z.; Chen, C.; Peng, Q.; Wang, D.; Li, Y., Enhanced oxygen reduction with single-atomic-site iron catalysts for a zinc-air battery and hydrogen-air fuel cell. *Nat Commun* 2018, *9* (1), 5422.
13. Chen, Y.; Ji, S.; Wang, Y.; Dong, J.; Chen, W.; Li, Z.; Shen, R.; Zheng, L.; Zhuang, Z.; Wang, D.; Li, Y., Isolated Single Iron Atoms Anchored on N-Doped Porous Carbon as an Efficient Electrocatalyst for the Oxygen Reduction Reaction. *Angewandte Chemie* 2017, *56* (24), 6937-6941.
14. Fei, H.; Dong, J.; Feng, Y.; Allen, C. S.; Wan, C.; Volosskiy, B.; Li, M.; Zhao, Z.; Wang, Y.; Sun, H.; An, P.; Chen, W.; Guo, Z.; Lee, C.; Chen, D.; Shakir, I.; Liu, M.; Hu, T.; Li, Y.; Kirkland, A. I.; Duan, X.; Huang, Y., General synthesis and definitive structural identification of MN4C4 single-atom catalysts with tunable electrocatalytic activities. *Nature Catalysis* 2018, *1* (1), 63-72.
15. Zhang, H.; Hwang, S.; Wang, M.; Feng, Z.; Karakalos, S.; Luo, L.; Qiao, Z.; Xie, X.; Wang, C.; Su, D.; Shao, Y.; Wu, G., Single Atomic Iron Catalysts for Oxygen Reduction in Acidic Media: Particle Size Control and Thermal Activation. *Journal of the American Chemical Society* 2017, *139* (40), 14143-14149.
16. Li, J.; Chen, M.; Cullen, D. A.; Hwang, S.; Wang, M.; Li, B.; Liu, K.; Karakalos, S.; Lucero, M.; Zhang, H.; Lei, C.; Xu, H.; Sterbinsky, G. E.; Feng, Z.; Su, D.; More, K. L.; Wang, G.; Wang, Z.; Wu, G., Atomically dispersed manganese catalysts for oxygen reduction in proton-exchange membrane fuel cells. *Nature Catalysis* 2018, *1* (12), 935-945.
17. Luo, F.; Roy, A.; Silvioli, L.; Cullen, D. A.; Zitolo, A.; Sougrati, M. T.; Oguz, I. C.; Mineva, T.; Teschner, D.; Wagner, S.; Wen, J.; Dionigi, F.; Kramm, U. I.; Rossmeisl, J.; Jaouen, F.; Strasser, P., P-block single-metal-site tin/nitrogen-doped carbon fuel cell cathode catalyst for oxygen reduction reaction. *Nature materials* 2020, *19* (11), 1215-1223.

18. Shao, Y.; Dodelet, J.-P.; Wu, G.; Zelenay, P., PGM-Free Cathode Catalysts for PEM Fuel Cells: A Mini-Review on Stability Challenges. *Advanced materials* 2019, *31* (31), 1807615.
19. Weiss, J.; Zhang, H.; Zelenay, P., Recent progress in the durability of Fe-N-C oxygen reduction electrocatalysts for polymer electrolyte fuel cells. *Journal of Electroanalytical Chemistry* 2020, *875*, 114696.
20. Miao, Z.; Li, S.; Priest, C.; Wang, T.; Wu, G.; Li, Q., Effective Approaches for Designing Stable M–Nx/C Oxygen–Reduction Catalysts for Proton-Exchange-Membrane Fuel Cells. *Advanced materials* 2022, *n/a* (n/a), 2200595.
21. Cui, C.; Gan, L.; Heggen, M.; Rudi, S.; Strasser, P., Compositional segregation in shaped Pt alloy nanoparticles and their structural behaviour during electrocatalysis. *Nature materials* 2013, *12* (8), 765-71.
22. Cui, C.; Ahmadi, M.; Behafarid, F.; Gan, L.; Neumann, M.; Heggen, M.; Cuenya, B. R.; Strasser, P., Shape-selected bimetallic nanoparticle electrocatalysts: evolution of their atomic-scale structure, chemical composition, and electrochemical reactivity under various chemical environments. *Faraday Discussions* 2013, *162*, 91.
23. Fu, X.; Liu, Y.; Cao, X.; Jin, J.; Liu, Q.; Zhang, J., FeCo–Nx embedded graphene as high performance catalysts for oxygen reduction reaction. *Applied Catalysis B: Environmental* 2013, *130-131*, 143-151.
24. Kodali, M.; Santoro, C.; Herrera, S.; Serov, A.; Atanassov, P., Bimetallic platinum group metal-free catalysts for high power generating microbial fuel cells. *Journal of power sources* 2017, *366*, 18-26.
25. Wang, J.; Huang, Z.; Liu, W.; Chang, C.; Tang, H.; Li, Z.; Chen, W.; Jia, C.; Yao, T.; Wei, S.; Wu, Y.; Li, Y., Design of N-Coordinated Dual-Metal Sites: A Stable and Active Pt-Free Catalyst for Acidic Oxygen Reduction Reaction. *Journal of the American Chemical Society* 2017, *139* (48), 17281-17284.
26. Kuang, M.; Wang, Q.; Han, P.; Zheng, G., Cu, Co-Embedded N-Enriched Mesoporous Carbon for Efficient Oxygen Reduction and Hydrogen Evolution Reactions. *Advanced Energy Materials* 2017, 1700193.
27. Onoda, A.; Tanaka, Y.; Matsumoto, K.; Ito, M.; Sakata, T.; Yasuda, H.; Hayashi, T., Bimetallic M/N/C catalysts prepared from π-expanded metal salen precursors toward an efficient oxygen reduction reaction. *RSC Advances* 2018, *8* (6), 2892-2899.
28. Herrmann, I.; Kramm, U. I.; Fiechter, S.; Bogdanoff, P., Oxalate supported pyrolysis of CoTMPP as electrocatalysts for the oxygen reduction reaction. *Electrochimica Acta* 2009, *54* (18), 4275-4287.
29. Serov, A.; Robson, M. H.; Smolnik, M.; Atanassov, P., Templated bi-metallic non-PGM catalysts for oxygen reduction. *Electrochimica Acta* 2012, *80*, 213-218.
30. Zhang, G.; Jia, Y.; Zhang, C.; Xiong, X.; Sun, K.; Chen, R.; Chen, W.; Kuang, Y.; Zheng, L.; Tang, H.; Liu, W.; Liu, J.; Sun, X.; Lin, W.-F.; Dai, H., A general route via formamide condensation to prepare atomically dispersed metal–nitrogen–carbon electrocatalysts for energy technologies. *Energy & Environmental Science* 2019, *12* (4), 1317-1325.
31. Li, S.; Zhang, L.; Kim, J.; Pan, M.; Shi, Z.; Zhang, J., Synthesis of carbon-supported binary FeCo–N non-noble metal electrocatalysts for the oxygen reduction reaction. *Electrochimica Acta* 2010, *55* (24), 7346-7353.
32. Galiote, N. A.; Oliveira, F. E. R.; Lima, F. H. B., FeCo-N-C oxygen reduction electrocatalysts: Activity of the different compounds produced during the synthesis via pyrolysis. *Applied Catalysis B: Environmental* 2019, *253*, 300-308.
33. Fang, H.; Huang, T.; Sun, Y.; Kang, B.; Liang, D.; Yao, S.; Yu, J.; Dinesh, M. M.; Wu, S.; Lee, J. Y.; Mao, S., Metal-organic framework-derived core-shell-structured nitrogen-doped CoCx/FeCo@C hybrid supported by reduced graphene oxide sheets as high performance bifunctional electrocatalysts for ORR and OER. *Journal of Catalysis* 2019, *371*, 185-195.
34. Wang, Z.; Ang, J.; Zhang, B.; Zhang, Y.; Ma, X. Y. D.; Yan, T.; Liu, J.; Che, B.; Huang, Y.; Lu, X., FeCo/FeCoNi/N-doped carbon nanotubes grafted polyhedron-derived hybrid fibers as bifunctional oxygen electrocatalysts for durable rechargeable zinc–air battery. *Applied Catalysis B: Environmental* 2019, *254*, 26-36.
35. Luo, F.; Wagner, S.; Onishi, I.; Selve, S.; Li, S.; Ju, W.; Wang, H.; Steinberg, J.; Thomas, A.; Kramm, U. I.; Strasser, P., Surface site density and utilization of platinum group metal (PGM)-free Fe–NC and FeNi–

NC electrocatalysts for the oxygen reduction reaction. *Chemical Science* 2021, *12*, 384-396.
36. Li, Y.; Shan, W.; Zachman, M. J.; Wang, M.; Hwang, S.; Tabassum, H.; Yang, J.; Yang, X.; Karakalos, S.; Feng, Z.; Wang, G.; Wu, G., Atomically Dispersed Dual-Metal Site Catalysts for Enhanced CO2 Reduction: Mechanistic Insight into Active Site Structures. *Angewandte Chemie International Edition* 2022, *61* (28), e202205632.
37. Yang, X.; Priest, C.; Hou, Y.; Wu, G., Atomically dispersed dual-metal-site PGM-free electrocatalysts for oxygen reduction reaction: Opportunities and challenges. *SusMat* 2022, *2* (5), 569-590.
38. Dong, F.; Wu, M.; Chen, Z.; Liu, X.; Zhang, G.; Qiao, J.; Sun, S., Atomically Dispersed Transition Metal-Nitrogen-Carbon Bifunctional Oxygen Electrocatalysts for Zinc-Air Batteries: Recent Advances and Future Perspectives. *Nano-Micro Letters* 2021, *14* (1), 36.
39. Mineva, T.; Matanovic, I.; Atanassov, P.; Sougrati, M.-T.; Stievano, L.; Clémancey, M.; Kochem, A.; Latour, J.-M.; Jaouen, F., Understanding Active Sites in Pyrolyzed Fe–N–C Catalysts for Fuel Cell Cathodes by Bridging Density Functional Theory Calculations and 57Fe Mössbauer Spectroscopy. *ACS Catalysis* 2019, *9* (10), 9359-9371.
40. Li, J.; Sougrati, M. T.; Zitolo, A.; Ablett, J. M.; Oğuz, I. C.; Mineva, T.; Matanovic, I.; Atanassov, P.; Huang, Y.; Zenyuk, I.; Di Cicco, A.; Kumar, K.; Dubau, L.; Maillard, F.; Dražić, G.; Jaouen, F., Identification of durable and non-durable FeNx sites in Fe–N–C materials for proton exchange membrane fuel cells. *Nature Catalysis* 2021, *4* (1), 10-19.
41. Ni, L.; Gallenkamp, C.; Paul, S.; Kübler, M.; Theis, P.; Chabbra, S.; Hofmann, K.; Bill, E.; Schnegg, A.; Albert, B.; Krewald, V.; Kramm, U. I., Active Site Identification in FeNC Catalysts and Their Assignment to the Oxygen Reduction Reaction Pathway by In Situ 57Fe Mössbauer Spectroscopy. *Advanced Energy and Sustainability Research* 2021, *2* (2), 2000064.
42. Jiao, L.; Li, J.; Richard, L. L.; Sun, Q.; Stracensky, T.; Liu, E.; Sougrati, M. T.; Zhao, Z.; Yang, F.; Zhong, S.; Xu, H.; Mukerjee, S.; Huang, Y.; Cullen, D. A.; Park, J. H.; Ferrandon, M.; Myers, D. J.; Jaouen, F.; Jia, Q., Chemical vapour deposition of Fe–N–C oxygen reduction catalysts with full utilization of dense Fe–N4 sites. *Nature materials* 2021, *20* (10), 1385-1391.
43. Concas, G.; Congiu, F.; Ennas, G.; Piccaluga, G.; Spano, G., Investigation of cobalt–iron alloy nanoparticles in silica matrix by X-ray diffraction and Mössbauer spectroscopy. *Journal of Non-Crystalline Solids* 2003, *330* (1), 234-241.
44. Leonard, N.; Ju, W.; Sinev, I.; Steinberg, J.; Luo, F.; Varela, A. S.; Roldan Cuenya, B.; Strasser, P., The chemical identity, state and structure of catalytically active centers during the electrochemical CO2 reduction on porous Fe–nitrogen–carbon (Fe–N–C) materials. *Chemical Science* 2018, *9* (22), 5064-5073.
45. Baur, W. H.; Khan, A. A., Rutile-type compounds. IV. SiO2, GeO2 and a comparison with other rutile-type structures. *Acta Crystallographica Section B* 1971, *27* (11), 2133-2139.
46. Chung, H. T.; Cullen, D. A.; Higgins, D.; Sneed, B. T.; Holby, E. F.; More, K. L.; Zelenay, P., Direct atomic-level insight into the active sites of a high-performance PGM-free ORR catalyst. *Science* 2017, *357* (6350), 479-484.
47. Gang Wu, Z. C., Kateryna Artyushkova, Fernando H. Garzon, and Piotr Zelenay, Polyaniline-derived non-precious catalyst for the polymer electrolyte fuel cell cathode. *ECS Transactions* 2008, *16* (2), 159-170.
48. Primbs, M.; Sun, Y.; Roy, A.; Malko, D.; Mehmood, A.; Sougrati, M.-T.; Blanchard, P.-Y.; Granozzi, G.; Kosmala, T.; Daniel, G.; Atanassov, P.; Sharman, J.; Durante, C.; Kucernak, A.; Jones, D.; Jaouen, F.; Strasser, P., Establishing reactivity descriptors for platinum group metal (PGM)-free Fe–N–C catalysts for PEM fuel cells. *Energy & Environmental Science* 2020, *13* (8), 2480-2500.
49. Jaouen, F.; Dodelet, J.-P., Average turn-over frequency of O2 electro-reduction for Fe/N/C and Co/N/C catalysts in PEFCs. *Electrochimica Acta* 2007, *52* (19), 5975-5984.
50. Bae, G.; Kim, H.; Choi, H.; Jeong, P.; Kim, D. H.; Kwon, H. C.; Lee, K.-S.; Choi, M.; Oh, H.-S.; Jaouen, F.; Choi, C. H., Quantification of Active Site Density and Turnover Frequency: From Single-Atom Metal to Nanoparticle Electrocatalysts. *JACS Au* 2021, *1* (5), 586-597.
51. Al-Zoubi, T.; Zhou, Y.; Yin, X.; Janicek, B. E.; Sun, C.-J.; Schulz, C. E.; Zhang, X.; Gewirth, A. A.; Huang, P. Y.; Zelenay, P.; Yang, H., Preparation of Non-precious Metal Electrocatalysts for the Reduction of Oxygen

Using a Low-Temperature Sacrificial Metal. *Journal of the American Chemical Society* 2020.
52. Leonard, N. D.; Wagner, S.; Luo, F.; Steinberg, J.; Ju, W.; Weidler, N.; Wang, H.; Kramm, U. I.; Strasser, P., Deconvolution of Utilization, Site Density, and Turnover Frequency of Fe–Nitrogen–Carbon Oxygen Reduction Reaction Catalysts Prepared with Secondary N-Precursors. *ACS Catalysis* 2018, *8* (3), 1640-1647.
53. Luo, F.; Choi, C. H.; Primbs, M. J. M.; Ju, W.; Li, S.; Leonard, N. D.; Thomas, A.; Jaouen, F.; Strasser, P., Accurate Evaluation of Active-Site Density (SD) and Turnover Frequency (TOF) of PGM-Free Metal–Nitrogen-Doped Carbon (MNC) Electrocatalysts using CO Cryo Adsorption. *ACS Catalysis* 2019, 4841-4852.
54. Sahraie, N. R.; Kramm, U. I.; Steinberg, J.; Zhang, Y.; Thomas, A.; Reier, T.; Paraknowitsch, J.-P.; Strasser, P., Quantifying the density and utilization of active sites in non-precious metal oxygen electroreduction catalysts. *Nature Communications* 2015, *6* (1), 8618.
55. Thompson, S. T.; Wilson, A. R.; Zelenay, P.; Myers, D. J.; More, K. L.; Neyerlin, K. C.; Papageorgopoulos, D., ElectroCat: DOE's approach to PGM-free catalyst and electrode R&D. *Solid State Ionics* 2018, *319*, 68-76.
56. http://www.crescendo-fuelcell.eu/?jjj=1577517876158, Official FCH JU Website for Project CRESCENDO, accessed 2023-06-09.
57. https://www.pegasus-pemfc.eu/, Official FCH JU Website for Project PEGASUS, accessed 2023-06-09
58. Li, J.; Jiao, L.; Wegener, E.; Richard, L. L.; Liu, E.; Zitolo, A.; Sougrati, M. T.; Mukerjee, S.; Zhao, Z.; Huang, Y.; Yang, F.; Zhong, S.; Xu, H.; Kropf, A. J.; Jaouen, F.; Myers, D. J.; Jia, Q., Evolution Pathway from Iron Compounds to Fe1(II)–N4 Sites through Gas-Phase Iron during Pyrolysis. *Journal of the American Chemical Society* 2020, *142* (3), 1417-1423.
59. Popov, N.; Ristić, M.; Bošković, M.; Perović, M.; Musić, S.; Stanković, D.; Krehula, S., Influence of Sn doping on the structural, magnetic, optical and photocatalytic properties of hematite (α-Fe2O3) nanoparticles. *Journal of Physics and Chemistry of Solids* 2022, *161*, 110372.
60. Akbar, A.; Bashir, S.; Riaz, S.; Naseem, S., Magnetic Properties of Co-doped Fe2O3 Thin Films. *Materials Today: Proceedings* 2015, *2* (10, Part B), 5674-5678.

For Table of Contents Only